Journal of Nondestructive Evaluation (2024) 43:65
https://doi.org/10.1007/s10921-024-01075-8

Selecting Feasible Trajectories for Robot-Based X-ray Tomography by Varying Focus-Detector-Distance in Space Restricted Environments

Maximilian Linde[1,2] · Wolfram Wiest[2] · Anna Trauth[1] · Markus G. R. Sause[1]

Received: 10 January 2024 / Accepted: 31 March 2024

Abstract
Computed tomography has evolved as an essential tool for non-destructive testing within the automotive industry. The application of robot-based computed tomography enables high-resolution CT inspections of components exceeding the dimensions accommodated by conventional systems. However, large-scale components, e.g. vehicle bodies, often exhibit trajectory-limiting elements. The utilization of conventional trajectories with constant Focus-Detector-Distances can lead to anisotropy in image data due to the inaccessibility of some angular directions. In this work, we introduce two approaches that are able to select suitable acquisitions point sets in scans of challenging to access regions through the integration of projections with varying Focus-Detector-Distances. The variable distances of the X-ray hardware enable the capability to navigate around collision structures, thus facilitating the scanning of absent angular directions. The initial approach incorporates collision-free viewpoints along a spherical trajectory, preserving the field of view by maintaining a constant ratio between the Focus-Object-Distance and the Object-Detector-Distance, while discreetly extending the Focus-Detector-Distance. The second methodology represents a more straightforward approach, enabling the scanning of angular sectors that were previously inaccessible on the conventional circular trajectory by circumventing the X-ray source around these collision elements. Both the qualitative and quantitative evaluations, contrasting classical trajectories characterized by constant Focus-Detector-Distances with the proposed techniques employing variable Focus-Detector-Distances, indicate that the developed methods improve the object structure interpretability for scans of limited accessibility.

Keywords Robot-based computed tomography · Limited accessibility · Distance variation

1 Introduction and Motivation

Computed tomography (CT) has developed into a fundamental tool in the area of non-destructive testing (NDT) in the automotive industry [1]. In conventional industrial CT-systems, the specimen under examination is positioned on a rotational manipulator situated between the X-ray source and the detector. However, the size of the specimen is constrained by both the sensitive detector region and especially the spatial limitations of the X-ray cabinet, necessitating the specimen's capability for rotation. Therefore, large components or partial regions within complete assemblies which exceed the size of the X-ray cabinet cannot be examined with standard systems. For high-resolution CT scans targeting specific regions on expansive components, such as complete automotive body structures, the utilization of robot-based CT presents a viable approach [2]. With this approach, the X-ray equipment is attached to collaborative industrial robots, allowing the implementation of versatile imaging geometries [3]. The six degrees of freedom available in robot-based CT have expanded the domain of seeking the optimal acquisition trajectory for an inspection task into a substantial field of research [4]. In addition to trajectory

✉ Maximilian Linde
maximilian.linde1@porsche.de

Wolfram Wiest
wolfram.wiest1@porsche.de

Anna Trauth
anna.trauth@mrm.uni-augsburg.de

Markus G. R. Sause
markus.sause@uni-a.de

[1] Institute of Materials Resource Management, University of Augsburg, Am Technologiezentrum 8, 86159 Augsburg, Germany

[2] Dr. Ing. h.c. F. Porsche AG, Porscheplatz 1, 70435 Stuttgart, Germany

Published online: 17 May 2024

optimization based on quality criteria along classical tilted orbits, the trajectory optimization from arbitrary views on a sphere, maintaining a constant Focus-Detector-Distance (FDD), is of particular importance [5–7]. The selection of the Focus-Object-Distance (FOD) and the FDD of such acquisition paths is typically chosen to ensure that the field of view (FOV) is large enough to capture the complete silhouette of the object in each X-ray projection image, thereby avoiding truncation. However, trajectories of constant FDD do not adequately address the problem of limited accessibility. The freedom of movement of the 6-axis robots in robot-based CT systems, and consequently the attainability of the imaging views, is frequently constrained by the presence of trajectory-limiting elements in the case of large-scale components. In instances where constraints arise from collisions, the angular range of the acquisition path can be severely limited, making it impossible to tangentially capture every object geometry in the inspection region with the X-ray beam [8]. This limitation precludes the generation of comprehensive datasets [9] in accordance with the Tuy-Smith sufficiency condition [10]. In order to leverage the potential of robot-based CT systems for inspecting hard-to-access regions, this work introduces the approach of using geometric distance variations of the X-ray imaging hardware. The objective is to improve the interpretability of object structures of scans in space restricted environments by integrating additional information through the integration of projections with varying FDDs. Two methods are pursued. Initially, view positions on spheres characterized by differing FDDs yet maintaining a constant FOV are reconstructed within a dataset. The goal of this *adaptive distance variation* is to incorporate additional view angles which could not have been integrated into a single sphere of views due to inaccessibility. The second methodology represents a more straightforward approach making previously inaccessible angular sectors on the classical circular trajectory scannable through the circumvention of the X-ray-source around collision elements. While the resulting projections with varying magnification deviate from the field of view of the basic dataset's projections, they can serve to supplement the deficient view directions.

2 State of the Art

The optimization of the source-detector trajectory in cone-beam CT is gaining growing significance across a broad spectrum of use-cases, including medical applications like interventional X-ray imaging [11] and industrial NDT applications [7]. Tailoring such trajectories to individual requirements by applying optimization functions enhances task-specific imaging performance. A detailed summary of the optimization of the source-detector trajectory in cone-beam CT as of 2022 is available in the existing literature [4]. Hence, the discussion of diverse optimization functions is omitted in this work. However, it is noticeable that the multitude of optimization algorithms is implemented using a constant FDD input dataset.

During scans conducted by robot-based CT in regions of large-scale components, a challenge manifests in the form of trajectory-limiting elements that often impede the accessibility of industrial robots. Absent a modification in either the FOD or the Object-Detector-Distance (ODD), the acquisition of views that are either unreachable or prone to collisions would simply not be feasible. In the domain of source-detector positioning optimization, scant endeavors have been directed towards the incorporation of variable FDDs.

Dabravolski implemented the *variable distance approach* (VDA) which optimally positions the X-ray source for each projection angle on a plane in proximity to the object according to its convex hull, while mitigating truncation effects. The FDD remains constant during the VDA. The findings indicate that this approach enhances both reconstruction quality and spatial resolution in elongated objects compared to standard circular trajectories [12]. A similar approach called *variable zoom technique* was presented by Nikishov. In this context, a variable FOD on a circular path is employed to obtain high resolution CT scans of regions in components characterized by large in-plane dimensions. Diverging from the VDA, an analytical reconstruction method closely aligning with the industry standard of the Feldkamp-Davis-Kress algorithm is utilized [13]. Both publications aim to improve the spatial resolution of regions through the application of optimized, non-constant FDDs on rotational trajectories within a plane. In both cases, constrained accessibility does not serve as a limiting factor. Given the restriction of slightly reduced spatial resolutions, employing a traditional circular trajectory would have remained a viable option.

Davis publication [14] utilizes circular trajectories of dynamic magnification, driven by the motivation to enable cone-beam CT imaging in image-guided radiation therapy. In the pursuit of maintaining a sufficient FOV, the ODD is dynamically increased to maintain clearance within an angular range around the potential collision of the patient and the machine. Davis's research demonstrates that these non-standard trajectories of inconsistent FDDs are essential for enabling imaging during impending collisions, while maintaining image quality comparable to standard circular CT.

Still, trajectories of varying FDDs on a two-dimensional plane inadequately harness the potential of robot-based CT in scenarios of limited accessibility. Edges of the test specimen, which cannot be captured tangentially by the X-ray beam despite dynamic magnifications due to trajectory-limiting elements along a direction in the two-dimensional plane, may be effectively captured by adopting a different viewpoint on the spherical surface. The authors are not aware of any methodologies in the domain of industrial CT for

implementing views of inconstant FDDs on a spherical input dataset to optimize scans with limited accessibility on large components. In this study, the *adaptive distance variation* method is introduced that optimizes the object structure interpretability in scans of limited accessibility by incorporating flexible FDDs on a spherical trajectory using a simulated robot-based CT. In addition, the method proposed by Davis is expanded to the application of robot-based CT. This signifies a more intuitive approach to trajectory planning in scenarios of limited accessibility and the adjustment of enlargement in collision-prone areas allows for the incorporation of additional sampling angles. A kinematized representation of a robot-based CT system (Digital Twin) facilitates collision and reachability assessments for the viewpoints utilized in the methodologies expounded in this manuscript.

3 Methodology

3.1 Strategies for Navigating Limited Accessibility

This section outlines the two methodologies employed in this study, designed to optimize robot-based CT scans under conditions of limited accessibility.

3.1.1 Adaptive Distance Variation—Maintaining the FOV while Modifying the FDD

The conceptual basis of this methodology involves the generation of multiple spherical X-ray acquisition view sets S characterized by a constant FOV and varying FDDs. This design enables the integration of supplementary, truncation free imaging views. In the case where certain angular ranges of the sampling sphere are precluded from a set of projections due to encountering collisions or robot inaccessibility, these angular intervals may be deemed permissible within an alternative set characterized by variable FDDs.

In this approach, the ratio of the FOD and the ODD is defined as follows:

$$\frac{FOD}{ODD} = const. \tag{1}$$

That guarantees uniformity in the FOV across all spherical view sets for their respective projections.

The subsequent procedure for specifying the distances between the X-ray hardware and the specimen of the various acquisition sets is explained in pseudo code in Table 1.

The parameterization of FDD_{max} must be user-controlled in an application-oriented manner. In addition to maintaining robot reachability, factors such as the maximum allowable exposure time (respectively scan duration) can also serve as decisive considerations for the parameterization of FDD_{max}.

In order to create a spherical sampling point cloud from the computed distance specifications of the individual view sets, an add-on tool was programmed for the *Delmia V5* robot simulation software (*Dassault Systèmes*) in collaboration with the *EngRoTec Consulting GmbH*. This tool facilitates the complete geometric parametrization of the spherical view sets. Furthermore, it enables the verification of the accessibility and collision-free status of sampling points by the robot, allowing for the exclusion of impermissible viewpoints. A more detailed description of the tool is provided in Sect. 3.2.

Subsequently, a cross-referencing process is conducted to match all admissible views across multiple view sets, mitigating the redundancy in capturing a projection angle. Throughout this procedure, a preference is consistently given to projections originating from sets with the smallest distances. This is done to minimize the necessary exposure time and mitigate the penetration of additional components as much as feasible. However, it is noteworthy that by preferring smaller FDDs, the influence of specimen scattering is amplified. The resulting set of viewpoints encompasses all accessible scanning positions along spheres with diverse radii while maintaining a constant FOV. The exposure time for projections is parametrized based on the set with the smallest distances and adapted to the subsequent sets through the application of the inverse square law:

$$D(r) = \frac{D_0}{r^2} \tag{2}$$

with r representing the distance from the radiation source and D representing the dose [15]. The parameterization of D_0 is configured by specialized CT personnel. Furthermore, a flat field correction is performed for each acquisition set. The exposure time is modulated as a variable control parameter across datasets, as we refrain from altering the acceleration voltage to avoid variations in the X-ray spectrum. Additionally, adjustments to the current are avoided, as this could influence the focal spot size and consequently the image sharpness.

3.1.2 Integrating Projections of Varying Magnification

The conventional circular trajectory represents the prevailing trajectory utilized in contemporary industrial NDT CT applications. A minimum of projections spanning 180° augmented by the cone beam aperture angle is requisite for the acquisition of a comprehensively defined dataset [16]. In instances where essential viewing perspectives are absent owing to restricted access to the testing area, this methodology provides an intuitive strategy to capture missing angular sectors by integrating projections of dynamic magnification.

Table 1 Pseudocode of the algorithm for specifying the geometric distances of the X-ray hardware for the subsequent creation of spherical acquisition sets of the *adaptive distance variation* approach

Pseudo code algorithm 1: Specification of the X-ray hardware distances of the spherical acquisition sets	
Input	
D_x, D_y [mm]	Detector dimensions in x and y directions
⌀ROI [mm]	Diameter of the region of interest (ROI)
α [°]	Opening angle of the X-Ray source
f	Distance variation factor
$\mathrm{FDD}_{\max}$ [mm]	Maximal permissible FDD
Output	
S	List S containing distance geometry information for all acquisition sets
Implementation	
If (⌀ROI > min(D_x, D_y)) then break	Truncation free projection of the ROI must be possible
$M_{\max} = \frac{\min(D_x, D_y)}{\varnothing \mathrm{ROI}}$	Determine the maximum achievable magnification $M_{\max}$ to achieve the finest possible voxel resolution
$\mathrm{FDD} = \frac{(\min(D_x, D_y) \cdot \frac{1}{2})}{\tan(\alpha)}$	Quantification of the minimal achievable FDD within the initial acquisition set
$\mathrm{FOD} = \frac{\mathrm{FDD}}{M_{\max}}$	Quantification of the minimal achievable FOD within the initial acquisition set
$\mathrm{ODD} = \mathrm{FDD} - \mathrm{FOD}$	Quantification of the minimal achievable ODD within the initial acquisition set
$i = 0$	Create an iterator
$S = []$	Generate a list for the parameters of the spherical acquisition sets
While ($\mathrm{FDD} \leq \mathrm{FDD}_{\max}$) do	Perform operations until the maximum allowable FDD is surpassed
$S[i] = [\mathrm{FDD}, \mathrm{FOD}, \mathrm{ODD}]$	Add the geometry data of the i^{th} spherical acquisition set to the list S
$\mathrm{ODD} = \mathrm{ODD} \cdot f$	Compute the ODD for the next spherical acquisition set
$\mathrm{FOD} = \mathrm{FOD} \cdot f$	Compute the FOD for the next spherical acquisition set
$\mathrm{FDD} = \mathrm{FOD} + \mathrm{ODD}$	Compute the FDD for the next spherical acquisition set
$i = i + 1$	Increment the iterator by 1
Save (S, "data location")	Save the list S at the location specified by the path ""data location"

The underlying methodology is straightforward. Initially, the process focuses on discerning the partial circular trajectory that maximizes the coverage of attainable angular ranges while maintaining a constant FOV. For this purpose, the output data from the sets generated by the *adaptive distance variation* method can be utilized. Partial circular trajectories covering a large potential scanning angle range as well as inaccessible angular ranges can be identified from the resulting X-ray source positions. The interpretation of the resulting polar coordinate plots of accessible source positions is described in Sect. 4.2.

To integrate the absent angular sectors into the trajectory, the FOD of the unreachable angular ranges is systematically enlarged until these regions become accessible:

$$min\{FOD_{new} | A(FOD_{new}) occurs, \; where\, FOD_{new} = FOD_{current} + n \cdot I \, for \, n \in \mathbb{N}\} \quad (3)$$

In this context, $\mathrm{FOD}_{\mathrm{new}}$ represents the sought FOD at which the state A (accessibility) occurs. This is achieved by incrementing $\mathrm{FOD}_{\mathrm{current}}$ n times by the distance increment I, which is defined by the user. Additionally, it is necessary to check whether the $\mathrm{FDD}_{\max}$ is exceeded. In the event of this occurrence, the ODD must be reduced iteratively until FDD $\leq \mathrm{FDD}_{\max}$:

$$ODD_{new} = max\{ODD_{current} - n \cdot K | FDD(ODD_{current} - n \cdot K) \leq FDD_{max} \, for \, n \in \mathbb{N}\} \quad (4)$$

Equation 4 encapsulates this procedural approach, where the variable K characterizes the subtracted distance constant. An analogous methodology involves augmenting the ODD within regions where the detector rotation is constrained. Nevertheless, our preference lies in the augmentation of the FOD, aiming to circumvent FOV truncation arising from the increasing magnification associated with the expansion of the ODD. Similar to the previous approach, a flat field correction is performed for each FDD configuration. In this approach as well, the X-ray exposure time, as specified in Equation 2, is

utilized as a variable parameter in the X-ray parameterization across sets of different distance configurations.

The presented techniques, as well as the notations of the distance abbreviations, are illustrated in Fig. 1. The ROI is located at the imaging isocenter. In this simple example, collisions of the source can be expected in the angular range of approximately 100° to 143° on the conventional circular trajectory in the depicted plane.

3.2 Simulation Framework Workflow

All simulations were conducted within the simulation framework depicted schematically in Fig. 2. The workflow is briefly outlined in the following.

Initially, sets of permissible radii for spherical view sets, as described in Sect. 3.1, are generated. This ideally facilitates the substitution of projection angle views that are inaccessible within a sampling point dataset with views derived from another dataset of varying radii. The resultant specifications pertaining to the distances of the X-ray hardware, in conjunction with the convex hull of the test object (STL data) and supplementary parameters for the parametrization of spherical trajectories, are incorporated into the commercially available process simulation software *DELMIA V5*. We employ an add-on tool (RCT-Tool) for *DELMIA V5*, specifically crafted for CT trajectory generation. In addition to trajectory parametrization, the tool has a cascade-like function for collision detection and accessibility control.

First, the tool incorporates a function for collision detection of the end effectors (X-ray source, X-ray detector and the static robot axis five and six). For this process, CAD models of existing X-ray sources and X-ray detectors as well as the connection to the robot axes five and six are applied to each viewpoint. Thus, viewpoints leading to collisions with the X-ray hardware are excluded. Subsequently, there is the option to subject the remaining valid viewpoints to a check for robot accessibility and collision of the robot with the component under investigation. The accessibility control is not yet automated in the current development status. Due to the large amount of data, accessibility checks were not used in the simulations of this work. It should therefore be noted that the sets of reachable views could be slightly smaller in reality. The output files contain all geometry information of the permissible sampling points, including cartesian coordinates delineating the position of the X-ray hardware, alongside Euler angles providing a description of its orientation. The data is systematically reported in tabular format.

Hence, like described in 3.1, the information is imported into the view selection algorithm to mitigate the occurrence of redundant capture angles across different sets. Thus, the geometric data of the sampling points in the acquisition set is established. In parallel, the material separated STL model of the test object is loaded into the X-ray simulation software *aRTist*. The X-ray parameterization in *aRTist* for this study is performed by the author, a specialized CT personnel. Using an automation script, X-ray projection images of the views from the acquisition set can be generated automatically. Finally, the simulated projection images, along with their corresponding projection matrices, are transferred to the *CERA 6* CT imaging software (*Siemens Healthineers AG*) for the reconstruction process. Given the limitation of analytical reconstruction methods reconstructing views of arbitrary perspectives, all data is reconstructed using the algebraic reconstruction technique (ART) inherent in the *CERA 6* CT imaging software. The ART is an iterative reconstruction method that considers the image as a solution to a linear system of equations. The iterative adjustment of the current image to the measured data minimizes the deviation between the measured and predicted data in each iteration. The ART included in the *CERA 6* CT imaging software allows the reconstruction of projections from arbitrary views while describing the acquisition geometry of each view through 3×4 projection matrices. These matrices are calculated for each view contained in the acquisition set. We opted for the *CERA 6* CT imaging software because of its robust programming interface designed for workflow automation and its capability to support projection matrix-based system geometry descriptions. In general, alternative CT reconstruction software that meets the described requirements can also be used. No significant alterations to the standard reconstruction parameters were required for the reconstructions.

3.2.1 Metrics Used for Quantitative Image Analysis

The quantitative assessment of the reconstructed datasets commences with a nominal-actual comparison, aligning the specific sets with the Ground Truth CAD model of the ROI within the commercially available CT-analysis software *VGSTUDIO MAX 2022.1* (*Volume Graphics GmbH*). This three-dimensional analysis provides an initial overview of the conformity between the reconstructed volumes and the Ground Truth. Furthermore, the analysis incorporates the metrics Structural Similarity Index (SSIM), Root Mean Squared Error (RMSE), and the Pearson Correlation Coefficient (PCC), which are applied to the cross-sectional images of the specific reconstructions. The combination of SSIM, RMSE, and PCC provides a comprehensive assessment of the similarity of cross-sectional images with a Ground Truth. The SSIM scrutinizes the structural distinctions inherent in a pair of images, mirroring the perceptual acuity of the human visual system towards structural variations [17]. The RMSE provides an average error metric, and the PCC enables the identification of linear relationships [18, 19]. The PCC provides an additional perspective on the similarity between the images in cases where the SSIM fails to accurately reflect

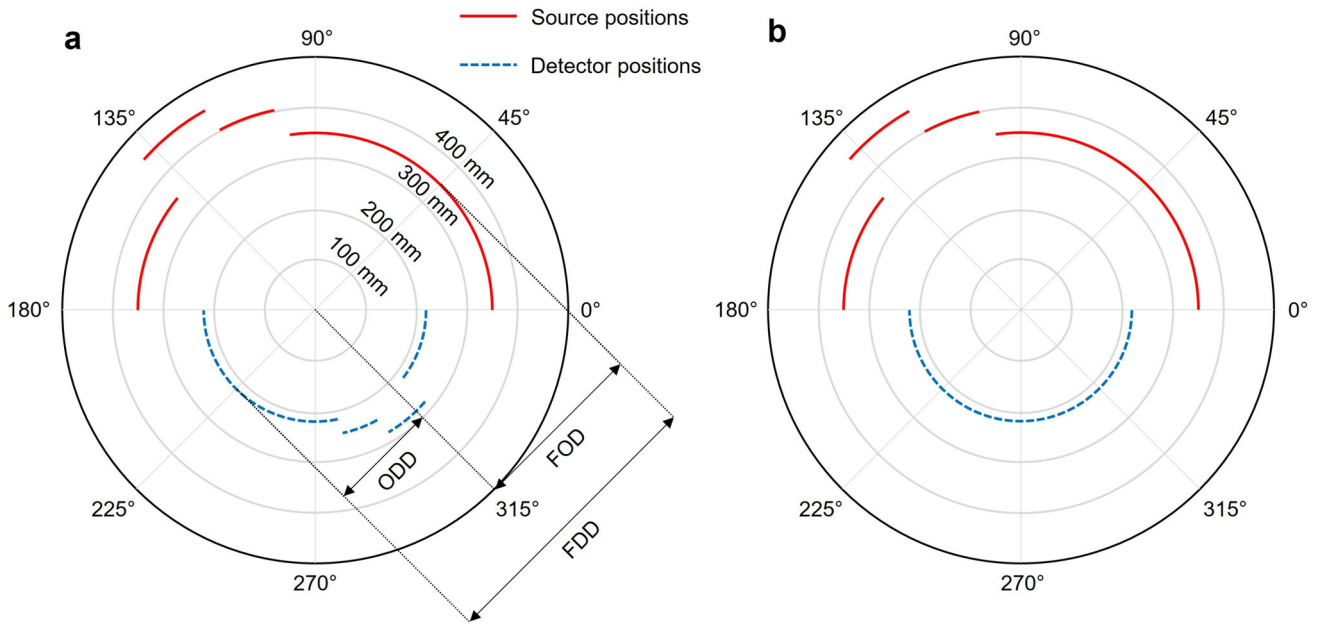

Fig. 1 Schematic two-dimensional representation of the *adaptive distance variation* approach (**a**). Collisions are circumvented through iteratively enlarged FDDs. The ratio between FOD and ODD remains constant. In a real scanning scenario, the approach is executed on the sphere (in three dimensions). The sub-image **b** illustrates the integration of dynamically enlarged projections in collision-prone areas on the conventional circular trajectory

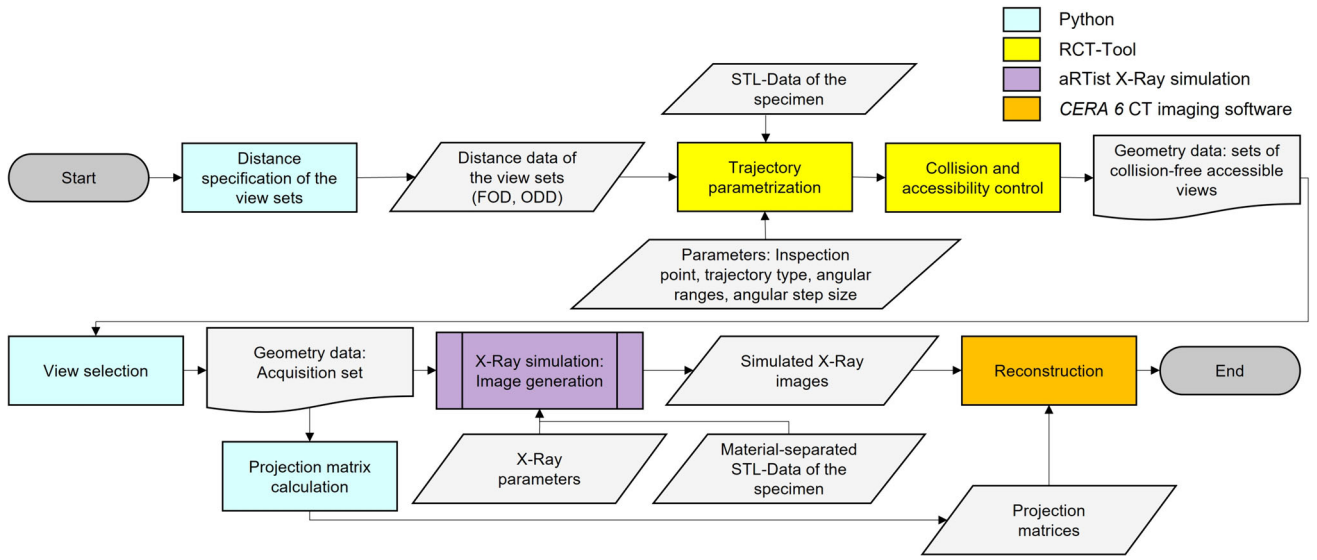

Fig. 2 Flowchart depicting the simulation framework employed in this study

the human perception of image similarity. There are studies in which the SSIM strongly differs from human observer perception of similarity between two images. It has been experimentally demonstrated that the PCC can better capture this similarity [18].

The SSIM values range from −1 to 1 with higher values indicative of higher correlation. However, instances of negative SSIM values are uncommon in typical application scenarios where relatively similar images are compared. The upper bound of the RMSE is constrained solely by the individual dynamic range of the pixel elements. A lower RMSE value signifies a closer proximity, on average, of pixel values within the images [19]. The PCC has a range of values from −1 to 1, where −1 corresponds to a negative linear correlation between the images, and 1 indicates a positive linear correlation. A higher Pearson correlation coefficient

indicates that the pixel values of the two images are more strongly correlated, suggesting a higher similarity [18]. The equations utilized for the computation of these metrics are delineated as follows:

$$SSIM(x,\ y) = \frac{(2\mu_x\mu_y + c_1)(2\sigma_{xy} + c_2)}{(\mu_x^2 + \mu_y^2 + c_1)(\sigma_x^2 + \sigma_y^2 + c_2)} \tag{5}$$

$$RMSE(x,\ y) = \sqrt{\frac{1}{n}\sum_{i=1}^{n}(x_i - y_i)^2} \tag{6}$$

$$PCC(x,\ y) = \frac{\sum_{i=1}^{n}(x_i - \mu_x)(y_i - \mu_y)}{\sqrt{\sum_{i=1}^{n}(x_i - \mu_x)^2 \sum_{i=1}^{n}(y_i - \mu_y)^2}} \tag{7}$$

In this context, μ_x and μ_y represent the mean values of the two images, while σ_x and σ_y denote the standard deviations of the images. The cross-covariance is expressed by σ_{xy} and constants c_1 and c_2 are introduced for the purpose of stabilizing the division. The variables n and i respectively describe the number of pixels and denote the iterator.

4 Simulations and Results

To illustrate the performance of the proposed methodology for optimizing robot-based CT scans of limited accessibility, measurements were simulated comparing acquisition sets on spherical paths with constant FDDs to acquisition sets with varying FDDs. As a ROI, a sector of a raw body structure in the area of the main beam facing the engine compartment on the driver's side was selected, cf. Fig 3. In these areas, there are challenging-to-access joint connections for CT examination. Due to the limitations in accurately depicting adhesive and screw connections in CAD, a test specimen comprising two aluminum sheets and self-piercing rivets was incorporated into the ROI.

For the purpose of demonstration, we try to accurately reconstruct the geometry of the rivets. In order to analyze the anisotropy of image data that often occurs in scans with limited accessibility due to the absence of projection angles, emphasis is placed on comparing the CT volumes and representative cross-sectional images of all three spatial levels.

The initial simulation delineates a comparative analysis between the proposed *adaptive distance variation* methodology and the conventional spherical acquisition path with constant FDDs. The subsequent simulation demonstrates how the integration of projections with varying magnification in inaccessible regions can provide additional data enhancements.

4.1 Approach 1: Adaptive Distance Variation—Maintaining the FOV while Modifying the FDD

Utilizing the algorithm detailed in Sect. 3.1, the X-ray hardware distances of the spherical acquisition sets are determined based on user-provided input parameters. These input parameters, along with the resulting output parameters of the algorithm, are presented in Table 2. The discretization factor f was assigned a value of 1.5 to avoid the main trajectory limiting elements with the resulting acquisition sets. To minimize the overall scanning duration, a maximum allowable exposure time of 2000 ms was set. Following the configuration of X-ray parameters, the resultant FDD_{max} was determined to be 1010.25 mm.

The corresponding acquisition sets are generated using the RCT-Tool, cf. Fig. 4a. Collision-prone acquisition points are systematically excluded using the tool. In this study, the evaluation of the kinematic chain accessibility for specific acquisition points is omitted due to limitations in the current developmental stage, which hampers efficient processing of the dataset's scale. However, the positioning of the object in the scene was chosen to ensure high accessibility. Additionally, the system geometry employed for the generation of the acquisition points is illustrated in Fig. 4.

The angular step size for sampling the data points was set to 5° in both the polar (θ) and azimuth (φ) angles. The resulting collision-free viewpoints of the three permissible acquisition sets are illustrated in Fig. 5.

The plots demonstrate that, depending on the acquisition set, different angular ranges can be sampled to varying degrees of completeness. Depending on the variation in distances, collisions occur in different angular ranges. It should be noted that a higher number of projections does not automatically yield better data. More valuable projections lead to better data quality. However, the inclusion of criteria regarding the quality of specific projection data is not the focus of this study. Instead, our aim is to investigate how the incorporation of additional view angles, which could not have been integrated into a standard trajectory of constant FDD due to inaccessibility, affects the imaging of a ROI.

As the X-ray hardware distance increases, additional collision-free viewpoints primarily emerge in the wheel housing and crossbeam struts area. Furthermore, at greater distances, the source exhibits an increased degree of mobility within the space delineated by the two main beams. Depending on the area, certain viewpoints also become inaccessible as the distance increases. The FDD of set 3 introduces vertical projection directions for the first time, as the crossbeam struts can be avoided. According to the description in Sect. 3.1, additional accessible views are now added to the acquisition set through a cross-referencing process. The set with the shortest distance serves as the initial basis due to the shortest

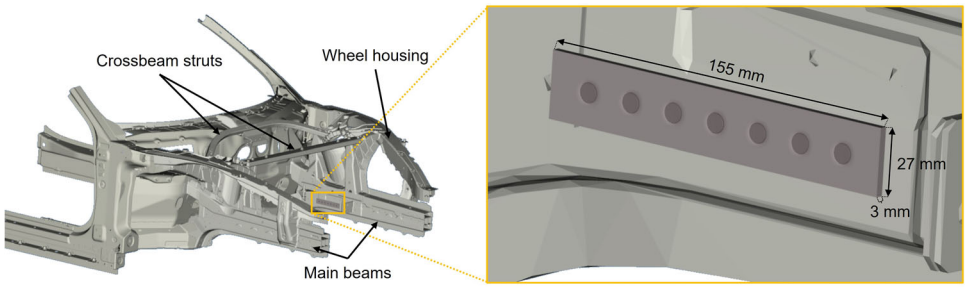

Fig. 3 ROI for the inspection task: self-piercing rivets near the main beam. Accessibility is significantly restricted by trajectory-limiting elements (main beams, crossbeam struts and wheel housing)

Table 2 Input and resulting output parameters of the spherical acquisition sets planning

Input parameters		Output parameters			
D_x, D_y [mm]	3000, 3000		FDD [mm]	FOD [mm]	ODD [mm]
⌀ROI [mm]	155	Set 1	412.1	213.0	199.1
α [°]	20	Set 2	618.2	319.5	298.7
f	1.5	Set 3	927.3	479.2	448.1
FDD_{max} [mm]	1010.25				

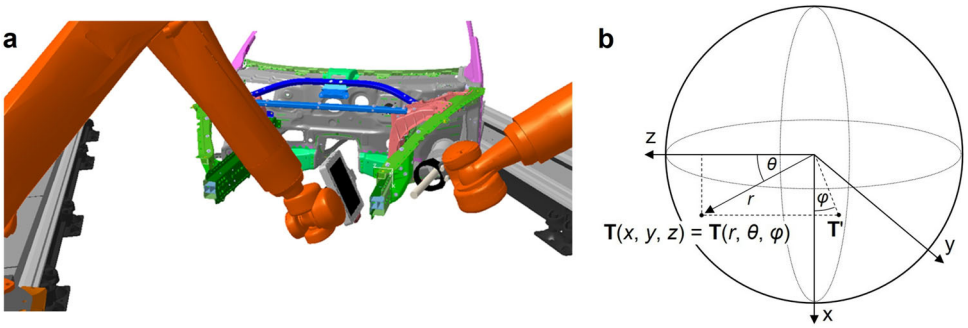

Fig. 4 RCT-Tool interface in *DELMIA V5* (**a**). System geometry of the acquisition point generation (**b**). Acquisition points $\mathbf{T} \in \mathbb{R}^3$ can be expressed in either cartesian or spherical coordinates. The subsequent plots adhere to the coordinate system convention illustrated herein

Table 3 Exposure times per projection of the acquisition sets. In the combined acquisition sets, the X-ray parametrization of the viewpoints is adjusted according to their respective originating set

Set	Exposure time [s]
Set 1 (blue)	0.333
Set 2 (yellow)	0.749
Set 3 (purple)	1.685

exposure time. For all imaging sets, the acceleration voltage is configured at 220 V, with a current of 0.2 mA and an average of 2. The pixel size is set to 0.1 mm. A 1 mm Cu filter is applied. The varying exposure times between sets are detailed in Table 3. It is important to note that the exposure times do not include robot movements and solely represent the imaging time. In the X-ray simulation, the complete raw body structure depicted in Fig. 3, including the embedded test specimen is incorporated with faithful to the original material representation.

The polar coordinate plots of the resulting combined acquisition sets are illustrated in Fig. 6.

In the following, the projections of the different sets were reconstructed into CT volumes using a voxel grid of 300 × 2500× 2500 with a voxel size of 0.1 mm.

Figure 7 depicts the sectional images of the resulting simulated volumes allowing for a qualitative assessment.

The reconstruction of set 1 fails to adequately depict the rivet head and the sheet metal edges. Upon comparing the associated views in Fig. 5, it becomes apparent that viewing directions capable of tangentially sampling the rivet head in the region of a polar angle of approximately 90° could not be pursued due to impending collisions. The contour of the rivet shaft is markedly more discernible. This is attributable to the fact that numerous viewing directions within the polar angle range of 0° to approximately 40° and 135° to approximately 180° were successfully captured. Also, the die side ends of the rivet shafts are not depictable due to similar missing viewing directions as with the rivet head. A similar observation is noted in the sectional images of set 2. The variation in distances between these sets did not allow for an additional rotation around a major trajectory-limiting element. Instead, it only facilitated the accessibility of individual viewpoints. In set 3, a significant improvement in the representation of

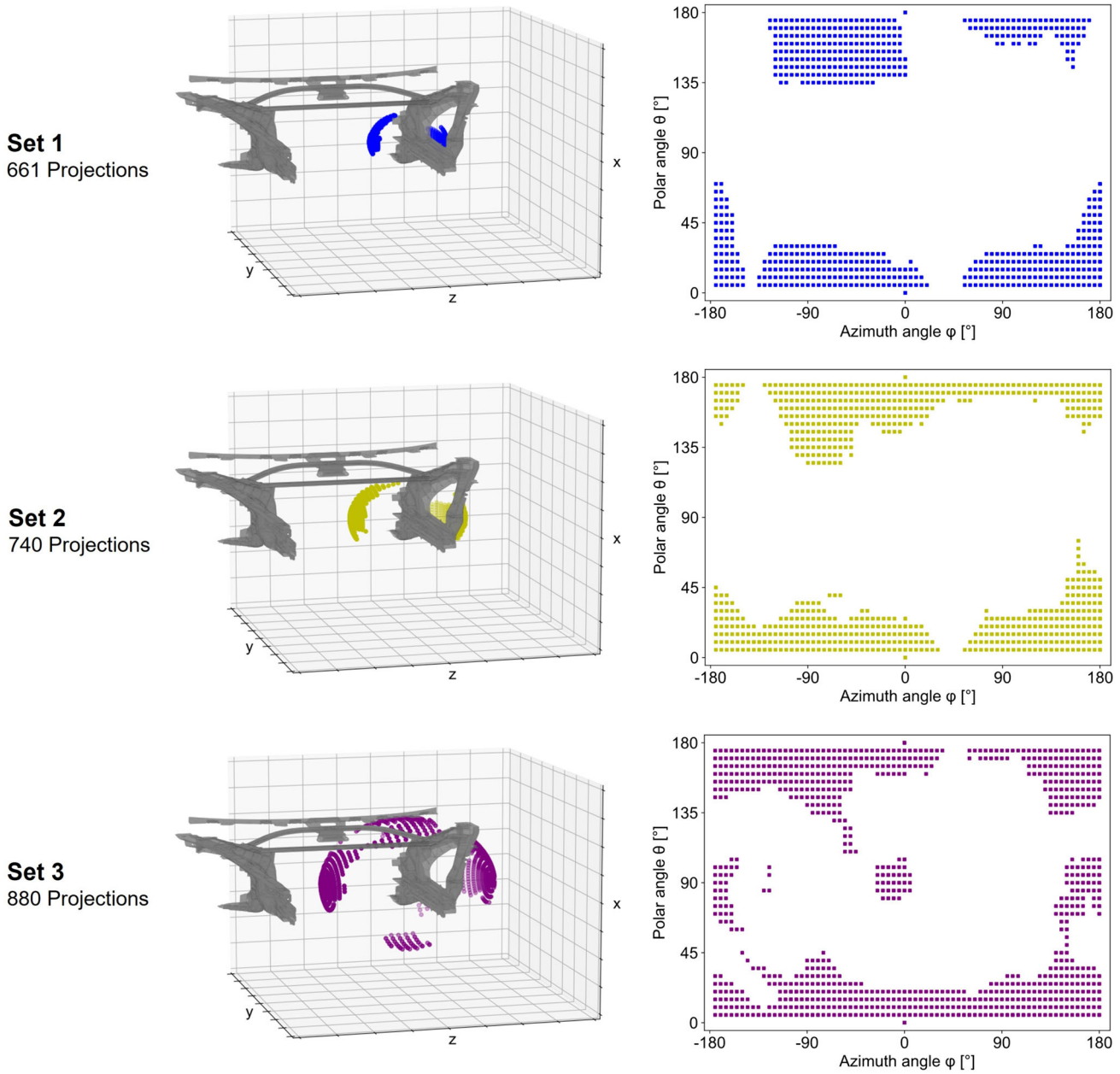

Fig. 5 Acquisition views of the source as a scatter plot in three-dimensional space including the relevant collision structures of the raw body structure and as a two-dimensional representation in spherical coordinates. The distance variation factor set with $f = 1.5$ is evident in the 3D plots

horizontal edges is discernible in both the sagittal and coronal sectional images. The comparison of the corresponding plots of viewing directions in Fig. 5 elucidates this observation, as with this set, viewpoints in the region of the polar angle of approximately 90° become accessible. Set 12 exhibits the same limitations as the originating sets 1 and 2. Set 123 combines the projections from sets 1 and set 2, which primarily depict the rivet shafts, with the projections from set 3, which predominantly depict edges along the direction of the rivet head. In comparison to set 3, set 123 exhibits a significantly shorter required exposure time, as projections with shorter exposure times from set 1 and set 2 can substitute a substantial portion of the projections in set 3. However, to draw conclusions regarding the comparison of the required scanning time, the robot manipulations would need to be considered which is not part of this work. The nominal-actual comparison of the reconstructed rivets with the Ground Truth CAD model presented in Fig. 8 underscores the interpretation of the CT sectional images once again.

Structures not tangentially sampled by X-rays in the sets do not provide valid information in the reconstruction and

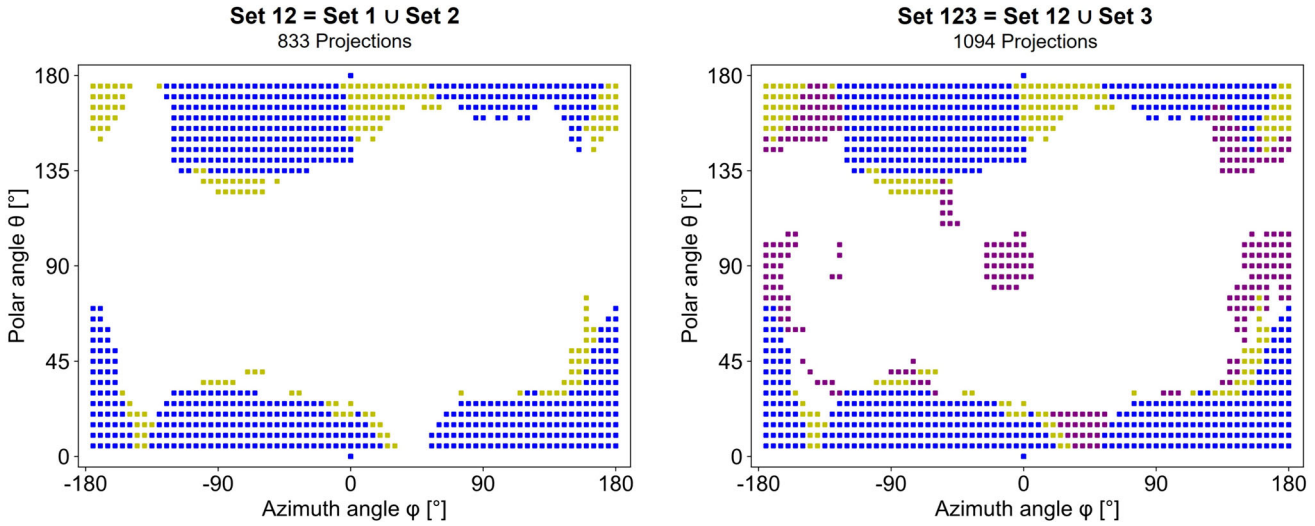

Fig. 6 Polar coordinate representation of the combined acquisition sets

consequently exhibit a high absolute deviation from the Ground Truth.

Quantitative image assessments of the different sets are provided in Table 4. Three 32-Bit float cross-sectional images of the central rivet with dimensions of 10 × 6 mm per set are utilized for the calculation of the metrics to incorporate analyses across all spatial directions. Only the central rivet is utilized for inspection, as the entire ROI is captured in each projection and truncation is prevented. Additionally, the expected theoretical object structure sampling of each rivet among one set is comparable as cone beam artifacts are avoided. The grayscale reference for the Ground Truth is an idealized, fully sampled simulated spherical reference scan of the ROI in which collisions were ignored. After registering the CAD model to this reference dataset, mean pixel intensities are computed for the rivets, metal sheets, and air regions through gray value analysis. The resulting Ground Truth was established by colorizing the CAD data based on the mean pixel intensities extracted from the reference scan. We chose the CAD as the ideal geometry due to its well-defined edges, with our focus on enhancing scan interpretability by incorporating additional structural object information. The influence of potential reconstruction artifacts on the object structure information can thus be minimized.

The SSIM observed in the transverse sectional images exhibits a lack of discernible pattern. This observation is consistent with the comparative analysis of the sectional images detailed in Fig. 7, as the human observer can detect all edges of the rivet shaft with similar accuracy. The sagittal and coronal sectional images demonstrate analogous trends in the SSIM values. The SSIM values increase proportionally with the augmentation of angular ranges sampled. This observation aligns with the qualitative analysis of the sectional images. The RMSE reveals marginal deviations in the transverse sectional images. Notably, set 123 exhibits an outlier in terms of its RMSE. In the sagittal and coronal sectional images, the RMSE displays distinctly elevated values in datasets characterized by a reduced number of angular perspectives. The investigation of linear correlation employing the PCC reaffirms the heightened similarity exhibited by sets encompassing larger sampled angular ranges when compared to the reference images. Again, it is notable that the transverse sectional images, especially in datasets with lower angular sampling, exhibit higher similarities with the Ground Truth compared to the sagittal and coronal planes. The behavior of the PCC in the sagittal and coronal sectional images aligns once again with the qualitative observations of the sectional images. The gradual transition of the gray values of the rivet within the inadequately represented rivet head region in sets 1, 2, and 12 contributes to a reduced PCC. The quantitative analysis of sagittal and coronal sectional images across various metrics demonstrates close correspondence in their respective values. The observed phenomenon arises from the complexity associated with the imaging geometry, where the direction of the rivet head plane poses the most challenging surface to scan due to potential collisions. The use of different test objects with varying motion restrictions of the X-ray hardware can lead to significant differences in the quantitative evaluation of these sectional planes.

4.2 Approach 2: Integrating Projections of Varying Magnification

This simulation is designed to showcase the enhancement of object structure interpretability in challenging accessibility scenarios using the conventional circular trajectory. By integrating projections of dynamic magnification within angular ranges traditionally inaccessible due to potential collisions,

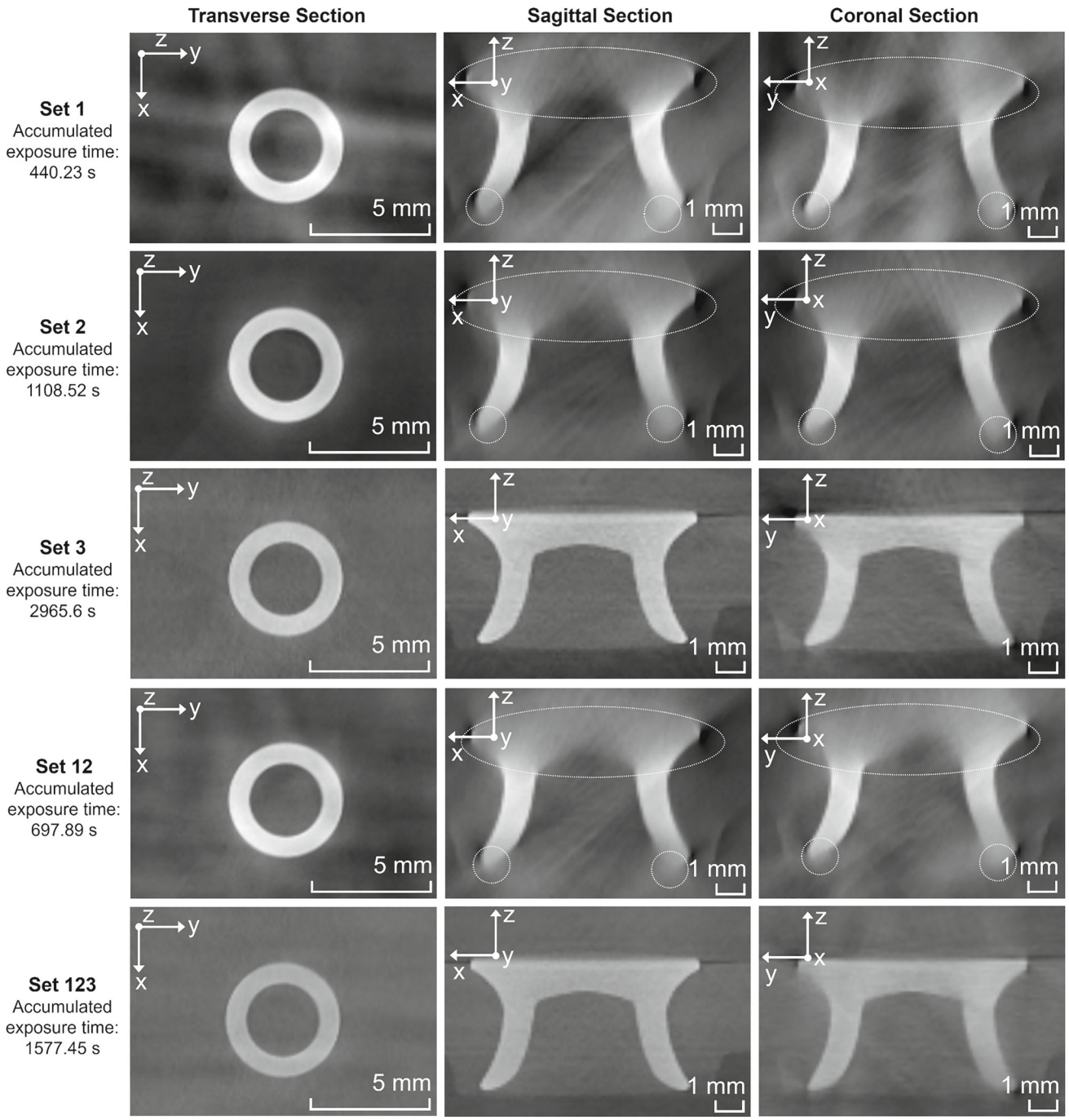

Fig. 7 Sectional images and the accumulated exposure time of the simulated CT volumes across all acquisition sets. Each sectional image depicts views through the central rivet

improvements in structural information content within specific regions of the FOV can be realized.

By leveraging the trajectory planning conducted in Sect. 4.1, the outcomes of this planning process are utilized for the execution of the present simulation. In Fig. 6, the right sub-image illustrates set 123, which represents the set containing the highest number of potential viewpoints without truncating the FOV. Circular trajectories can be inferred from this data. Vertical lines in the plot (constant azimuth angle φ) describe a semicircle, which is completed by the corresponding vertical line at $\varphi = 180°$ apart to form the full circular trajectory. The corresponding polar angle ranges of $\varphi = 0°$ and $\varphi = 180°$ delineate the circular trajectory in the XZ-plane. The rotation of this trajectory around the Z-axis is identified by the azimuth angles being shifted by an equivalent magnitude in the plot.

Table 4 Quantitative analysis of data quality across all datasets of simulation 1

	SSIM			RMSE			PCC		
	Transverse section	Sagittal section	Coronal section	Transverse section	Sagittal section	Coronal section	Transverse section	Sagittal section	Coronal section
Set 1	0.5437	0.3567	0.3539	0.0326	0.0783	0.0793	0.9543	0.6418	0.6412
Set 2	0.6137	0.3977	0.3631	0.0299	0.0716	0.0735	0.9781	0.7384	0.7266
Set 3	0.6044	0.4641	0.4795	0.0223	0.0459	0.0375	0.9854	0.9396	0.9623
Set 12	0.5960	0.4141	0.3721	0.0299	0.0691	0.0690	0.9679	0.7480	0.7665
Set 123	0.5267	0.5200	0.5460	0.0571	0.0520	0.0479	0.9810	0.9478	0.9581

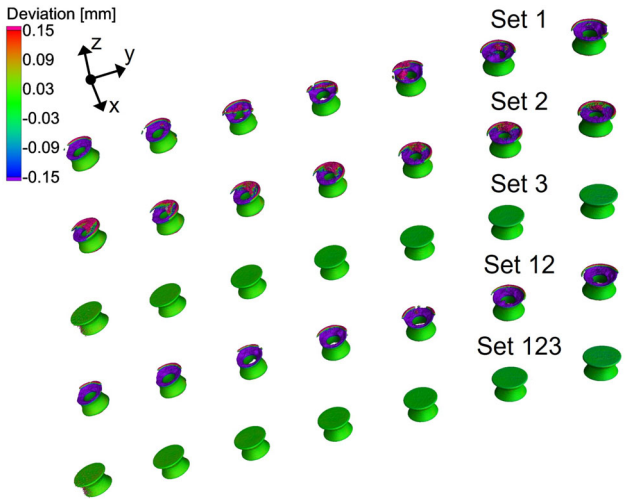

Fig. 8 3D rendering of the nominal-actual comparison of the simulated CT volumes (rivets) with the CAD Ground Truth. The surface determination required for nominal-actual comparison was conducted using the *advanced surface determination* methodology integrated within *VGSTUDIO MAX 2022.1*, with a search radius of 0.4 mm/4 voxels, without additional cleaning or repairing steps. The best fit registration method was employed for volume-to-CAD registration

The presented data in Fig. 6 indicates that the circular trajectory in the XZ-plane covers most of the polar angle range. The resulting trajectory, illustrated in Fig. 9 therefore serves as the initial data set for this simulation. This set is referred to as set 123C. No contiguous arc segment within set 123C satisfies the required condition of a sampling angle of at least 180° plus the cone beam aperture angle to result in a complete dataset. It is evident that no observations could be captured within the region $\varphi = 0°; \theta = 30°$ to 80° because of the impending collision between the detector and the wheel housing. Additionally, the angular range $\varphi = 0°; \theta = 110°$ to 135° could not be accessed due to the impending collision of the detector with the crossbeam struts. The last inaccessible angular range $\varphi = 180°; \theta = 110°$ to 140° remains unobstructed due to insufficient FOD in the region of the wheel housing. In this simulation, as described in Sect. 3.1, the FOD in the RCT-Tool is systematically increased, until achieving conditions enabling the rotation of the X-ray source around the wheel housing. The resulting trajectory of set 123C, as well as the viewpoints of additional dynamically magnified projections in set 4C, are computationally modeled under constant X-ray parameters. Modifications are confined to the exposure time of set 4C's projections, according to Eq. 2.

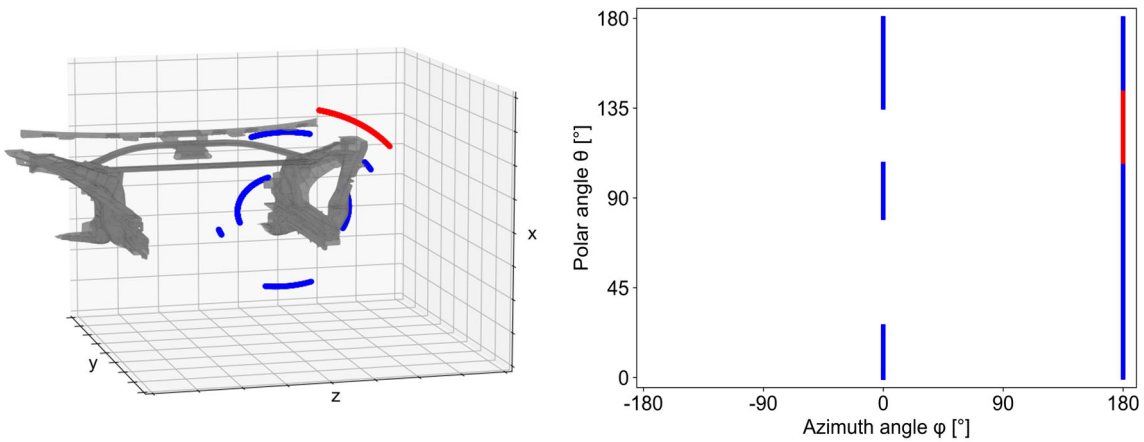

Fig. 9 Illustration of the initial set "set 123C" in blue. The corresponding, missing angular sectors for a complete trajectory are marked in red (set 4C). The fusion of acquisition points results in set 1234C

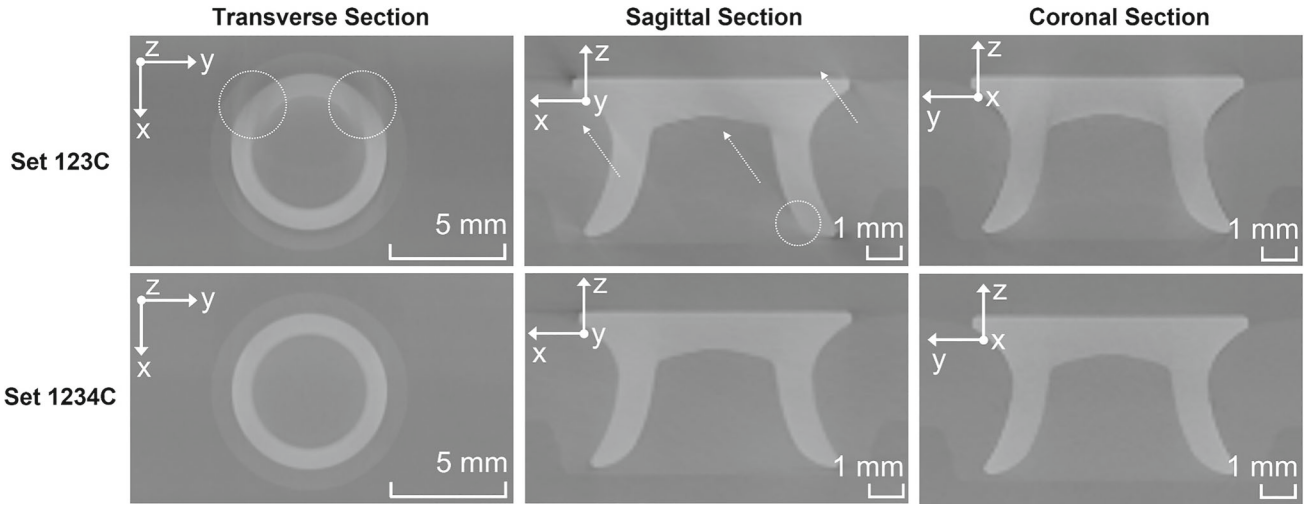

Fig. 10 Comparison of sectional images from the resulting simulated CT volumes. Each sectional image depicts views through the central rivet. Missing projection angles result in artifacts in the sectional images of set 123C

The angular step size of the acquisition views is set to 0.1°, in order to adhere to the rule of thumb that the number of projections should approximately match the number of horizontal detector elements [20].

Table 5 provides a comprehensive overview of the parameterization applied to the supplementary projections of varying magnification in set 4C.

In the following, the projections of the different sets are reconstructed into CT volumes of the same parametrization like in 4.1. Figure 10 depicts the sectional images of the resulting simulated volumes allowing for a qualitative assessment.

The transverse sectional image of set 123C clearly illustrates the effects of the missing projection directions. Missing wedge artifacts can be observed in the upper third of the transverse sectional image of the rivet shaft. Particularly evident in the sagittal cross-sectional image are edges characterized by a degree of blurring, exhibiting an orientation along lines extending approximately from 5 to 11 o.clock positions. Notably, the internal contour of the die-facing end of the rivet shaft exhibits pronounced artifacts. The presented artifacts arise because of deficient sampling angle coverage in $\varphi = 180°; \theta = 110°$ to 140° respectively $\varphi = 0°; \theta = 40°$ to 70°. These are the only missing angular ranges that cannot be sampled by an opposing reachable view direction on the full circle. The sectional images of set 1234C do not exhibit any artifacts stemming from inadequate angular sampling.

The comparison between the reconstructed rivets and the Ground Truth CAD model in Fig. 11 emphasizes the interpretation of the CT sectional images.

In regions affected by missing wedge artifacts along the absent projection directions, dataset 123C exhibits significant variations from the Ground Truth. Through the integration of projections with varying magnifications, the dataset 1234C is now completely sampled, eliminating any missing wedge artifacts. As a result, there are almost no deviations from the CAD. Quantitative image assessments of the sets are provided in Table 6. The procedure is identical to that described in Sect. 4.1.

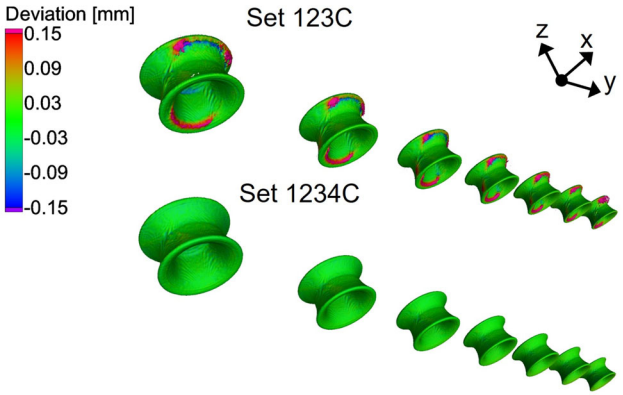

Fig. 11 3D rendering of the nominal-actual comparison of the simulated CT volumes (rivets) with the CAD Ground Truth. The data generation process is identical to that depicted in Fig. 8

It becomes evident that set 1234C can exhibit significantly higher SSIM values in all images compared to set 123C. It is noticeable that the SSIM of the sagittal sectional image of set 123C appears small compared to the qualitative analysis. Furthermore, the RMSE of the trajectory entirely sampled through projections of dynamic magnification, exhibits a significantly reduced value. Additionally, the observed patterns in the PCC of dataset 1234C in comparison to dataset 123C, especially in the transverse section, underline the impression of better object structure interpretability.

Table 5 Parametrization of the supplementary dynamically magnified projections

Set	FDD [mm]	FOD [mm]	ODD [mm]	Exposure time [s]
Set 4C (red)	1010.25	630.0	380.2	2

Table 6 Quantitative analysis of data quality across all datasets of simulation 2

	SSIM			RMSE			PCC		
	Transverse section	Sagittal section	Coronal section	Transverse section	Sagittal section	Coronal section	Transverse section	Sagittal section	Coronal section
Set 123C	0.3048	0.1818	0.3427	0.0556	0.0688	0.0540	0.9483	0.9400	0.9229
Set 1234C	0.6029	0.5472	0.5475	0.0196	0.0339	0.0350	0.9803	0.9478	0.9438

4.3 Comparison and Practicability of the Approaches

Both presented approaches enable a more comprehensive representation of object geometries compared to trajectories of constant FDDs by integrating additional projection angles of varying FDDs. The sphere-based *adaptive distance variation* technique has some advantages over the circle-based integration of projections with varying magnifications. With an identical FDD configuration, there are scenarios, in which it can enable the sampling of object areas that are not reachable on the circular trajectory. This is because projections from other directions can substitute for the information loss of the missing circular projections. Such a scenario can be observed when comparing the transverse section of set 123 (see Fig. 7) with that of set 123C in Fig. 10. While the sectional image of the rivet shaft in the circle-based approach does not fully depict the geometry, these artifacts can be avoided by the sphere-based approach. Furthermore, the selection of the optimal starting basis (circle tilt) represents an additional effort in the circle-based methodology, which significantly impacts imaging. The *adaptive distance variation* technique is independent of such influence. Of course, it should be noted that for some scenarios, the circle-based approach remains the simpler and faster implementation. This methodology can theoretically be easily configured through manual trajectory parameterization. Furthermore, the projection data from the circle-based approach could also be reconstructed using filtered back projection (FBP). On a projection basis, preprocessing would be necessary due to the dynamic magnifications. With the sphere-based approach, algebraic reconstruction methods need to be employed.

5 Conclusion

Robot-based CT presents a groundbreaking opportunity for the high-resolution examination of ROIs in large-scale components such as e.g. HV battery frames, vehicle bodies or casting elements. Due to trajectory-limiting elements of the structures, such scans typically exhibit limited accessibilities for the X-ray hardware and the industrial robots. Hence, it constitutes an exception that the classical circular trajectory can be adequately realized as an acquisition trajectory. The introduction of spherical acquisition sets, as demonstrated in e.g. [21], encounters analogous challenges attributable to impending collision concerns.

In this study, we present two methodologies capable of sampling additional acquisition directions by integrating projections at varying distances of the X-ray hardware through the circumvention of trajectory-limiting elements. For this purpose, we have devised a simulation solution that features an automated computation of collision-free viewpoints, based on the convex hull of the object to be examined. This tool is coupled with an interface to a database, facilitating the loading of diverse components.

The *adaptive distance variation* approach integrates collision-free viewpoints on a spherical trajectory, preserving the FOV by maintaining a constant ratio between FOD and ODD, while discretely expanding the FDD. The second methodology represents a more straightforward approach making previously inaccessible angular sectors on the classical circular trajectory scannable through the circumvention of the X-ray-source around these collision elements. The ensuing projections of varied magnification and the spherical trajectories from the first method, are reconstructed utilizing an ART, facilitated by the provision of 3×4 projection matrices for each imaging geometry.

The methodologies were validated for a challenging to access junction situated within the area of the main beam of an automotive body structure. Both the qualitative and quantitative comparison of classical trajectories with constant FDDs and the proposed techniques with variable FDDs demonstrate that the developed methods can achieve higher object structure interpretability than conventional approaches. It must be noted that the SSIM can provide unreliable values for blurred images [22]. This could explain

the behavior of the low SSIM value in the sagittal sectional image of set 123C, although the qualitative analysis by the human observer would yield a higher result. In summary, the combined statement of the metrics used, and the qualitative assessment clearly reflect the added value of the presented methods.

It is highly challenging to generate evaluable data in restricted accessibility environments. The presented methods entail a relatively high effort for scanning individual components. However. they are able to capture additional structural object information gain. Generally, robot-based CT scans involve a relatively high trajectory planning effort compared to conventional systems. In regions with limited accessibility, this effort increases further due to trajectory-limiting collision structures. Consequently, being able to apply such a trajectory multiple times (mass inspection) is always advantageous. However, the approach demonstrated can also be implemented for individual scans, as these methodologies may potentially ensure the interpretability of the scan.

The utilization of a smaller-scaled distance variation factor would further increase the time expenditure. However, it is plausible that the inclusion of additional sampling points, if they can contribute to addressing still missing viewing directions within the trajectory, may potentially enhance the interpretability of a scan. Similar behavior can be anticipated with the increase of the constraint on the maximum allowable FDD. Optimizing robot path planning is beyond the scope of this study. However, its absence does not diminish the demonstrated additional value achieved through the proposed techniques.

The additional integration of metrics that check the data quality of individual projections into the presented workflow could further secure or even improve the scans. Furthermore, the implementation of quality criteria evaluating the informative content of projections specific to each inspection task has the potential to achieve substantial time efficiency without compromising image quality. Particularly in the few-view online/atline inspection scenario, the combination of the presented methodology and the incorporation of quality criteria could open new domains for robot-based CT, enabling the acquisition of fast CT scans from challenging-to-access regions.

Author Contributions ML: conceptualization, methodology, implementation, data generation, data analysis, writing – original draft preparation; WW: data analysis, review and editing; AT: Scientific discussion, review and editing; MS: Scientific discussion, review and editing.

Funding This work was funded by the Dr. Ing. h.c. F. Porsche AG and facilitated through collaborative research between academia and industry in partnership with the University of Augsburg. The method presented is not currently available for commercial use, and there is no assurance of its future availability.

Declarations

Conflict of Interest The authors have no relevant financial or non-financial interests to disclose.

Code Availability Not applicable.

References

1. Withers, P.J., Bouman, C., Carmignato, S., et al.: X-ray computed tomography. Nature Reviews Methods Primers (2021). https://doi.org/10.1038/s43586-021-00015-4
2. Ziertmann A., Jahnke P., Holub W.: RoboCT - Production Monitoring in Automobile Industry 4.0. Sonderband ZfP heute:22–26 (2020).
3. Bauer, F., Forndran, D., Schromm, T., et al.: Practical part-specific trajectory optimization for robot-guided inspection via computed tomography. J. Nondestr. Eval. **41**, 55 (2022). https://doi.org/10.1007/s10921-022-00888-9
4. Hatamikia, S., Biguri, A., Herl, G., et al.: Source-detector trajectory optimization in cone-beam computed tomography a comprehensive review on today's state-of-the-art. Phys. Med. Biol. **67**, 16TR03 (2022). https://doi.org/10.1088/1361-6560/ac8590
5. Bauer, F., Goldhammer, M., Grosse, C.U.: Selection and evaluation of spherical acquisition trajectories for industrial computed tomography. Proc. R. Soc. A. (2021). https://doi.org/10.1098/rspa.2021.0192
6. Schneider L-S., Thies M., Schielein R., et al.: Learning-based Trajectory Optimization for a Twin Robotic CT System (2023).
7. Herl, G., Hiller, J., Thies, M., et al.: Task-specific trajectory optimisation for twin-robotic X-Ray tomography. IEEE Transactions on computational imaging **7**, 894–907 (2021). https://doi.org/10.1109/TCI.2021.3102824
8. Barutcu, S., Aslan, S., Katsaggelos, A.K., et al.: Limited-angle computed tomography with deep image and physics priors. Sci. Rep. **11**, 17740 (2021). https://doi.org/10.1038/s41598-021-97226-2
9. Quinto, E.T.: Singularities of the X-Ray transform and limited data tomography in R^2 and R^3. SIAM J. Math. Anal. **24**, 1215–1225 (1993). https://doi.org/10.1137/0524069
10. Tuy, H.K.: An inversion formula for cone-beam reconstruction. SIAM J. Appl. Math. **43**, 546–552 (1983). https://doi.org/10.1137/0143035
11. Stayman, J.W., Capostagno, S., Gang, G.J., et al.: Task-driven source–detector trajectories in cone-beam computed tomography: I. theory and methods. Journal of Medical Imaging **6**, 25002 (2019). https://doi.org/10.1117/1.JMI.6.2.025002
12. Dabravolski, A., Batenburg, K.J., Sijbers, J.: Adaptive zooming in X-ray computed tomography. J. Xray Sci. Technol. **22**, 77–89 (2014). https://doi.org/10.3233/XST-130410

13. Nikishkov, Y., Kuksenko, D., Makeev, A.: Variable zoom technique for X-ray computed tomography. NDT and E Int. **116**, 102310 (2020). https://doi.org/10.1016/j.ndteint.2020.102310
14. Davis, A.M., Pearson, E.A., Pan, X., et al.: Collision-avoiding imaging trajectories for linac mounted cone-beam CT. J. Xray Sci. Technol.Technol. **27**, 1–16 (2019). https://doi.org/10.3233/XST-180401
15. Krieger, H. (ed.): Strahlungsmessung und Dosimetrie. Springer Fachmedien Wiesbaden, Wiesbaden (2021)
16. Kalender, W.A.: Computed Tomography: Fundamentals, System Technology, Image Quality, Applications, 3rd edn. Publicis Publishing, Erlangen (2011)
17. Zhou Wang, A.C., BovikSheikh, H.R., et al.: Image quality assessment: from error visibility to structural similarity. IEEE Trans. Image Process. **13**, 600–612 (2004). https://doi.org/10.1109/TIP.2003.819861
18. Starovoytov, V.V., Eldarova, E.E., Iskakov, K.T., et al.: Comparative analysis of the SSIM index and the Pearson coefficient as a criterion for image similarity. Eurasian Journal of Mathematical and Computer Applications **8**, 76–90 (2020). https://doi.org/10.32523/2306-6172-2020-8-1-76-90
19. Umme, S., Morium, A., Mohammad Shorif, U.: Image quality assessment through FSIM, SSIM, MSE and PSNR-A comparative study. Journal of Computer and Communications **7**(3), 8–18 (2019). https://doi.org/10.4236/jcc.2019.73002
20. Buzug, T. (ed.): Computed Tomography: From Photon Statistics to Modern Cone-Beam CT. Springer, Berlin Heidelberg, Berlin, Heidelberg (2008)
21. Herl, G., Hiller, J., Maier, A.: Scanning trajectory optimisation using a quantitative tuybased local quality estimation for robot-based X-ray computed tomography. Nondestructive Testing and Evaluation **35**, 287–303 (2020). https://doi.org/10.1080/10589759.2020.1774579
22. Guan-Hao Chen., Chun-Ling Yang., Lai-Man Po., et al.: Edge-Based Structural Similarity for Image Quality Assessment. In: 2006 IEEE International Conference on Acoustics Speech and Signal Processing Proceedings, II-II (2006).